Technology and image results of a spectral CT system

B.J. Heismann[*], S. Wirth, S. Janssen, Q. Spreiter

Siemens Medical Solutions, Computed Tomography Detector Center, Siemensstr. 1,
91301 Forchheim, Germany

ABSTRACT

We report the implementation and first test results of a two-channel spectral Computed Tomography (CT) prototype. We use an energy-resolving CT detector with a sandwich-like two layer set-up. Compared to dual-energy approaches with tube voltage switching, it yields a low and a high energy channel in a one shot measurement. We explain the basic set-up of the system and its calibration. The effects of spectral weighting are examined and the weighting functions $w(E)$ of the detector channels are calculated. We present spectral image data of a water phantom, a set of calibration materials and an organic sample. Finally, we show how the data can be used for quantitative CT measurements. The system is work in progress and currently not available in the United States.

Keywords: Computed tomography, spectral resolution, ρZ projection

INTRODUCTION

State-of-the-art medical CT measurements yield precise information on the attenuation coefficient $\mu(r)$ of the human body. While the spatial resolution has been increased steadily into the sub-millimeter range in the last few years, spectral resolution is currently not commercially used. This is probably based on the fact that its straight-forward applications are not of key interest in CT. Unlike in SPECT or PET, background events have not to be sorted out by energy discrimination, since they are negligible compared to the x-ray flux. Scatter reduction would be a useful feature, but it requires a very precise energy measurement and probably a monochromatic x-ray source.

However, the roots of spectral CT extend well into the 'pre-spiral' age. Kalender et al. [1] used a tube-voltage switching technique in the commercially available SOMATOM DR (Siemens, Germany, 1983-1987). A pulsed tube with alternating voltage settings between adjacent projections created a set of dual energy data. An approach based on pre-reconstruction base-material decomposition [1,2] was used to generate pairs of high and low Z material images such as 'bone' and 'soft-tissue'. This option served well for some applications like bone-densiometry [3].

With the rise of spiral technology, x-ray tubes shifted to continuous radiation. This was the main reason that the dual-energy option was no longer implemented. In this paper we will present the first realization of an energy-resolving CT system based on detector technology.

EXPERIMENTAL SET-UP

In order to facilitate the assembly of our spectral CT system, we used a Somatom Emotion duo CT (Siemens Medical Solutions, Forchheim, Germany) as a platform. We exchanged the standard two-slice detector modules with our sandwiched spectral modules. Figure 1 shows a photographic representation and Fig. 2 the schematics of the assembly. Basically we have taken two standard single-slice modules and put them on top of each other. The UFC scintillator thickness of the top module was reduced to 200μm, while the lower module preserved the standard 1.4 mm. A standard antiscatter collimator was attached to the top module.

---

[*] electronic mail: bjoern.heismann@siemens.com

In operation, x-ray quanta partly cross the first scintillator layer and are absorbed in the second layer. The upper level tends to pick up the lower energy quanta whereas the lower level absorbs preferably the remaining high-energy quanta. Since we now have two energy channels instead of two slices per detector element, the total number of measurement channels stays constant. Therefore we can use the standard detector read-out electronics. With minor adjustments to the positional z control of the x-ray tube, we end up with a fully functional spectral CT system.

THEORY

Current CT systems measure the distribution of the attenuation coefficient $\mu(r)$.

μ is determined by applying a Radon transformation to a set of measured projections $I/I_0(n)=P(n)$. It is usually normalized to the dimensionless Hounsfield value

$$C = 1000 \frac{\mu - \mu_{Water}}{\mu_{Water}}. \quad (1)$$

The spectral weighting of μ in first order approximation of the Lambert Beer law is given by

$$\mu = \int w(E)\kappa(E)dE. \quad (2)$$

Here, $\kappa(E)$ is the spectral attenuation coefficient at energy E and $w(E)$ is the weighting function

$$w(E) = \frac{S(E)D(E)}{\int S(E)D(E)dE}, \quad (3)$$

with the spectrum $S(E)$ in quanta per second at energy E and the detector absorption probability $D(E)$ with $0 < D(E) < 1$.

Fig 3 shows $S(E)$ and $D(E)$ for the standard Emotion Duo 130kV mode. For our spectral system, we measure two μ_1, μ_2 with different spectral weightings w_1, w_2. In order to calculate these functions, we have modelled our detector system according to Fig. 2. The intermediate absorbing layers like the module substrates or the scintillator reflective paint (see Fig. 1) were treated according to the proposals of Rowlands and Taylor [4], assuming that half the photons scattered in these layers are scattered forward into the detector.

Fig. 4 shows the resulting w_1 and w_2. The top layer obviously absorbs the majority of the low-energy quanta. The bottom layer receives the high-energy dominated rest of the quanta.

The measured μ_1 and μ_2 data can now be used for spectral CT methods like the base material decomposition [1-3] and the pZ projection [5]. Since the latter will be used to interpret some of the experimental results, we shortly revise this method and its main results:

The pZ projection converts two measurements of μ_1, μ_2 with different spectral weighting w_1, w_2 into density $\rho(r)$ and atomic number $Z(r)$ information.

$$\begin{pmatrix} \mu_1(\rho, Z) \\ \mu_2(\rho, Z) \end{pmatrix} \rightarrow \begin{pmatrix} \rho(\mu_1, \mu_2) \\ Z(\mu_1, \mu_2) \end{pmatrix} \quad (4)$$

[5] provides both analytical and numerical solutions to that problem. We have to invert

$$\begin{pmatrix} \mu_1 \\ \mu_2 \end{pmatrix} = \rho \cdot \begin{pmatrix} \int w_1(E)\left(\dfrac{\kappa}{\rho}\right)(E,Z)dE \\ \int w_2(E)\left(\dfrac{\kappa}{\rho}\right)(E,Z)dE \end{pmatrix} = \rho \begin{pmatrix} f_1(Z) \\ f_2(Z) \end{pmatrix} \quad (5)$$

for ρ and Z. This yields

$$Z = F^{-1}\left(\frac{\mu_1}{\mu_2}\right), \quad (6)$$

$$\rho = \frac{\mu_1}{f_1(Z)} = \frac{\mu_1}{f_1\left(F^{-1}\left(\dfrac{\mu_1}{\mu_2}\right)\right)} \quad (7)$$

as the numerical solution with

$$f_i(Z) = \int w_i(E)\left(\frac{\kappa}{\rho}\right)(E,Z)\,dE, \quad (8)$$

$$F(Z) = \frac{f_1(Z)}{f_2(Z)}. \quad (9)$$

RESULTS AND DISCUSSION

In order to calibrate the spectral CT system we started with a standard 30cm water phantom measurement. Fig. 5a,b show the corresponding images for both layers. The water image of layer 1 has standard noise level and distribution. For layer 2 we notice periodic rotational artifacts. This is explained by a small portion of primary radiation (up to 2%) which passes through the scintillator septa of layer 1 and hits layer 2 directly. The angle of inclination increases towards the edges of each module in angular (φ) direction. This creates the periodic rotational pattern with an underestimation of $C(\mu_2)$ of up to -20HU for sharp reconstruction kernels. This shortcoming can be overcome by either shielding of the septa in layer 1 or a numerical correction of the raw measurement data. In this paper we present the intermediate results based on uncorrected system data.

Material	ρ /gcm^{-3}	ρ /gcm^{-3} (meas.)	Z	Z (meas.)
C	1.74	1.58	6	6.12
N (liquid)	0.81	0.73	7	7.39

Table 1: Theoretical and measured density and atomic number of the calibration materials carbon and (liquid) nitrogen

As the next step, we scanned samples of the pure elements carbon (Z = 6) and liquid nitrogen (Z = 7). We applied the ρZ projection according to (6,7) to the data, using the $w_{1,2}$ of Fig. 4. The resulting values for the theoretical density and atomic number and the measurement results are shown in Table 1. The atomic numbers are reproduced with a deviation of +0.12 and +0.39, whereas the density is underestimated by –0.16 g/cm^3 and –0.12 g/cm^3. This is below the precision

of $\Delta Z = +/-0.1$ and $\Delta\rho = +/-0.02 g/cm^3$ reached for the dual-voltage method in [5]. The larger deviation is probably due to the underestimation of μ_2 discussed above: $F^{-1}(x)$ in (6) is a monotone increasing function of $x = \mu_1/\mu_2$. Thus, a reduced μ_2 yields an increased x and Z.

Finally, we took cross sectional images of a pig's spine region as an organic sample for muscle, fat and vertebral bone tissue. Fig. 6a shows an overview image taken with layer 1. We have chosen a window center $c_s = 400$ HU and a width of $w_s = 2500$ HU in order to depict the full dynamics. Fig. 6b shows a zoomed representation with $[c_s = 0$ HU , $w_s = 400$ HU], this time taken with layer 2. We have used a medium reconstruction kernel in order to reduce the artifacts described above. Fig. 6c and d show the ρZ projected zoom of the organic sample. We have used a ρ window of $[c_s = 1.20$ g/cm^3 , $w_s = 0.75$ g/cm^3] and a Z window of $[c_s = 9.0$, $w_s = 7.5]$.

The darker regions in both the ρ and Z image correspond to fat embedded in muscle flesh. We have two bone structures in the arc-shaped, cracked white structure on the lower right and the triangle shaped form on the right. Though smoothed out by magnification, we can see structures in both the fat/muscle and the inner bone regions that are not easily distinguished in the original Fig. 6a,b). The main reason for this is the reduction of dynamics from the high-range attenuation coefficient to the compressed scale of ρ and Z. The detailed structures can not be attributed to the artifacts in Fig. 5b) since they would occur with different orientation at their position relative to the center.

Comparing the Z and ρ for the bone structures reveals some interesting details. For the right triangular shaped bone, e.g., we have a rise of Z from Z=10.9 to 11.9 from the center to the edges, whereas the density ρ is more heterogeneously distributed between 1.1 and 1.65 g/cm^3. Table 2 summarizes the overall intervals of measured values for bone, muscle and fat pig tissue. We can extract values for comparable human cell classes from [6], see table 3. The effective Z is calculated according to a Z^3 averaging weighted with the partial chemical densities (see [5]). According to the results of the calibration test, the measured Z values for muscle and fat will be overestimated by around +0.2. However, even if we do not expect a full coincidence, the values fit into the observed intervals.

	$\rho/g cm^{-3}$ (meas.)	Z (meas.)
Vertebral bone (pig)	1.10 ... 1.80	10.9 ... 13.0
Muscle (pig)	1.03 ... 1.11	7.5 ... 8.7
Fat (pig)	0.92 ... 1.00	5.9 ... 6.4

Table 2: Measured density and atomic number for the cell material types in Fig. 6.

	$\rho/g cm^{-3}$ (ICRU 46 [6])	Z (approx)
Vertebral column, adult	1.42	11.6
Muscle, adult	1.05	7.7
Lipoma	0.98	6.3

Table 3: Tissue densities and approximated effective atomic numbers [5,6].

SUMMARY

A spectral CT prototype system has been constructed, calibrated and tested. We have calculated the spectral weighting functions of the two energy channels. Image data of a water phantom, pure materials and an organic sample of a pig's spine region has been generated. We have transformed the latter two images into distributions of the density ρ and atomic number Z using the ρZ projection algorithm. The quantitative results are in principal agreement with the expected density and atomic number of the pure materials. For carbon, we obtain a deviation of +0.12 in Z and -0.16 g/cm^3 in ρ, for liquid nitrogen we have a difference of +0.39 for Z and -0.12 g/cm^3 for ρ. A numerical correction to the

primary radiation incident on layer 2 will probably lead to a further improved precision. The images of the organic sample show that we can identify and examine typical body tissues like muscle, fat and bone tissue. We find a good similarity between the measured quantitative values for a pig and the human equivalent tissue types.

ACKNOWLEDGEMENTS

REFERENCES

[1] W.A. Kalender W.H. Perman , J.R:Vetter, E. Klotz, Evaluation of a prototype dual-energy computed tomographic apparatus. I. Phantom studies, Med Phys. **13(3)**, 334. (1986)

[2] R.E: Alvarez and A Macovski, Energy-selective reconstructions in X-ray computerised tomography . Phys. Med. Biol. **21**, 733 (1976)

[3] W.A: Kalender, E. Klotz, C. Suess,. Vertebral bone mineral analysis: an integrated approach with CT. Radiology **164(2)**, 419. (1987)

[4] J. A. Rowlands and K. W. Taylor, Absorption and noise in cesium iodide x-ray image intensifiers, Med. Phys. **10**, 786, (1983)

[5] B. J. Heismann, J. Leppert and K. Stierstorfer, Density and atomic number measurements with spectral x-ray attenuation method, Jour. Appl.. Phys **94(3)**, 2073 (2003)

[6] ICRU, International Commission on Radiation Units and Measurements **46**, (1992)

Fig. 1. Photo of the sandwiched module. We have combined two standard single-slice modules with mechanical spacers to one spectral module. It has two energy channels per pixel.
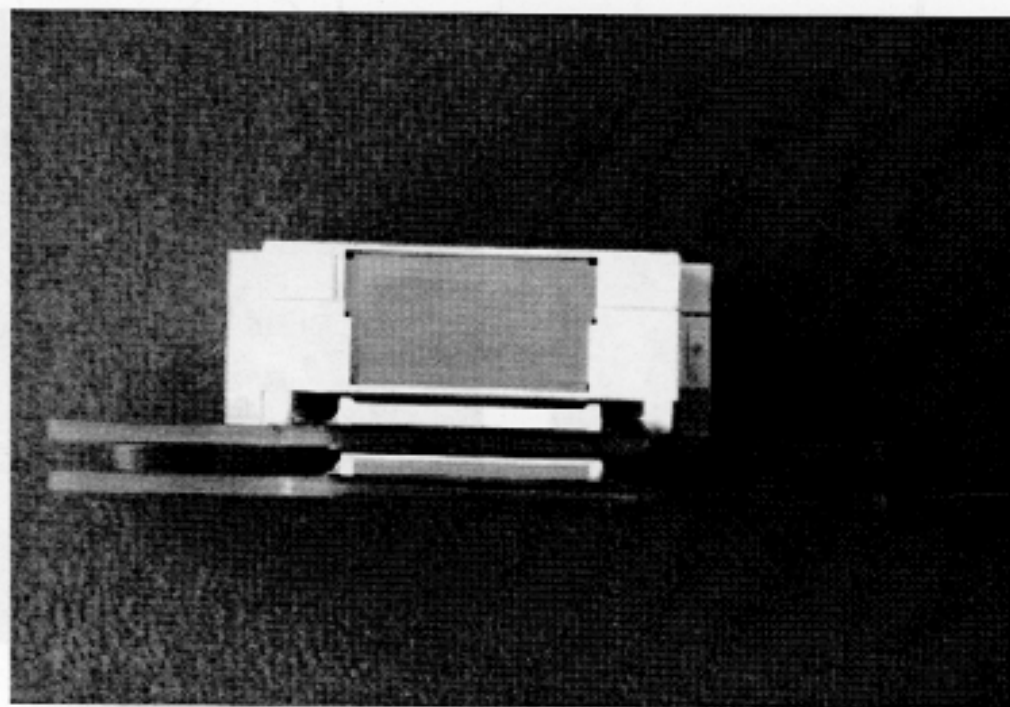

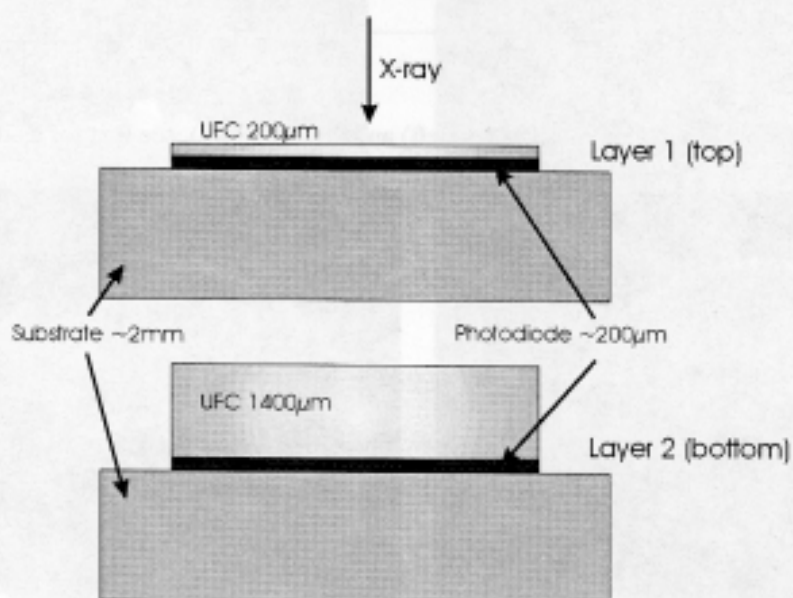Fig. 2. Schematics of the module set-up.

Fig.3 a,b. Standard 130kV spectrum $S(E)$ and detector absorption probability $D(E)$ for a Somatom Emotion Duo.
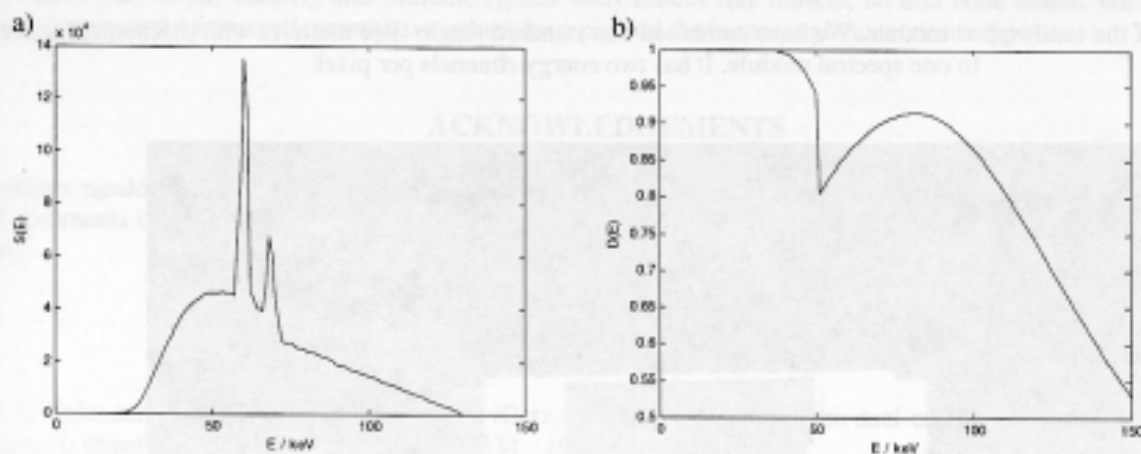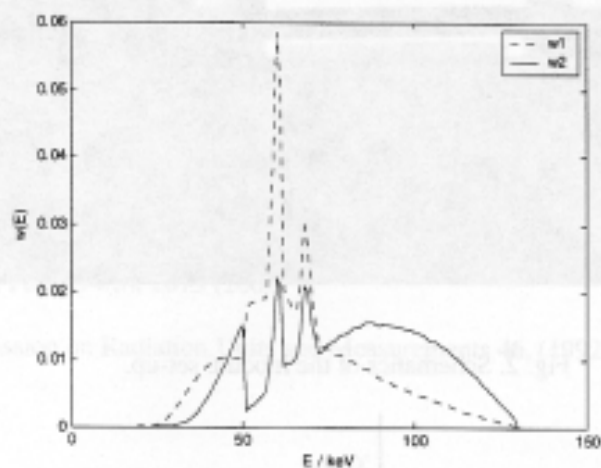
a)

b)

Fig. 4.: $w_{1,2}$ of the two detector layers.

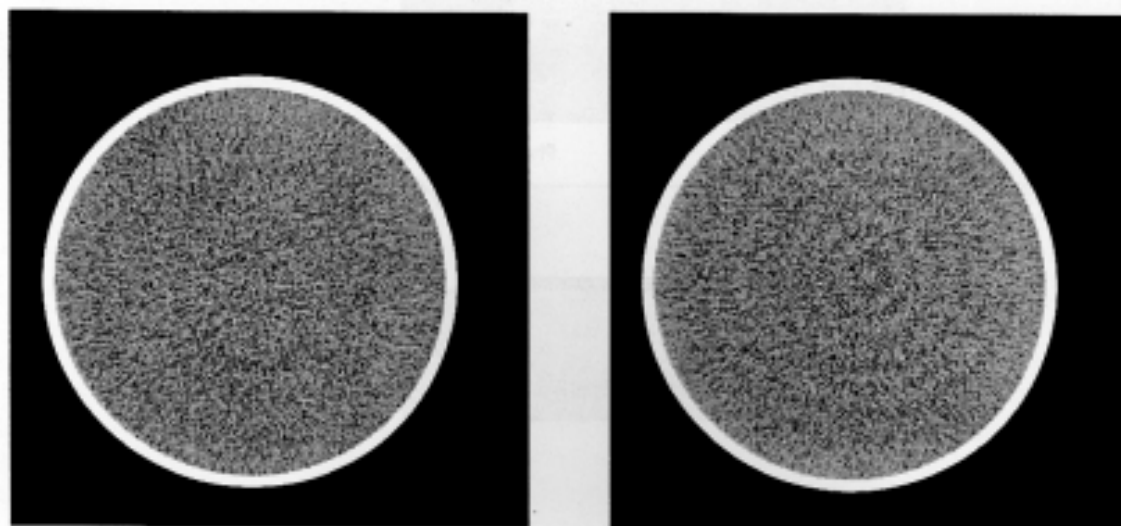Fig .5. Water phantom images of layer 1 (left) and layer 2 (right), see text for analysis.
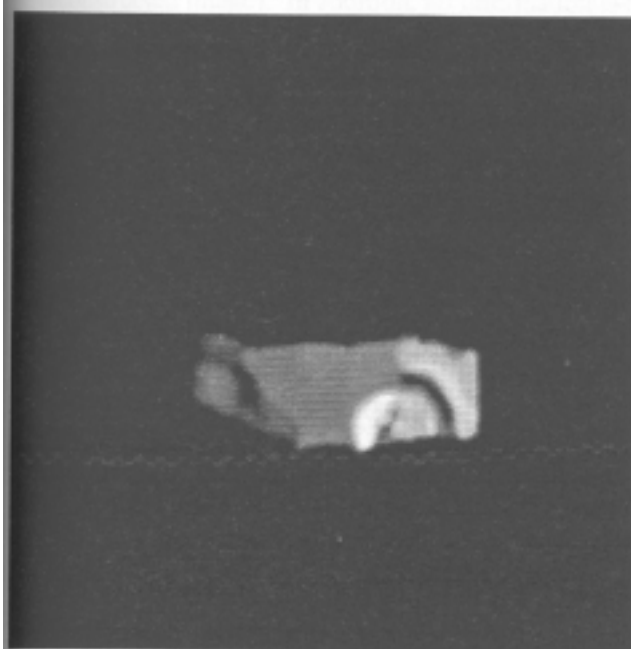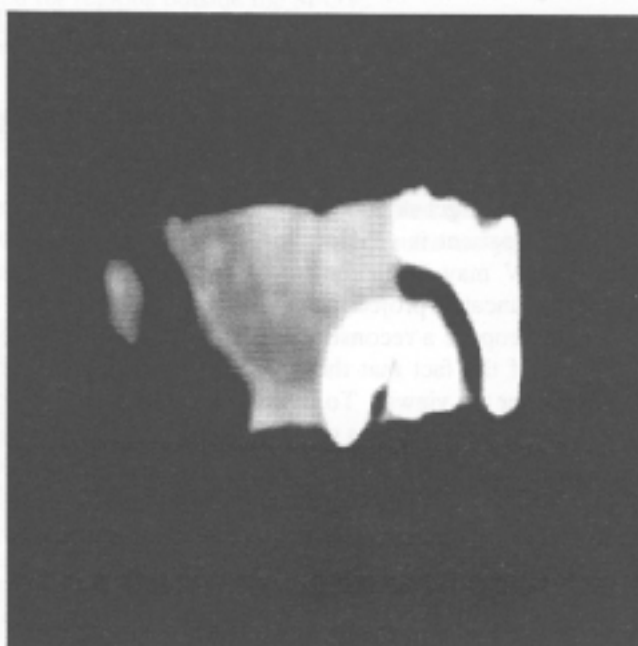
Fig. 6 Image series of an organic sample (pig spine region). The respective center c_s and width w_s of the gray scale images are stated below.
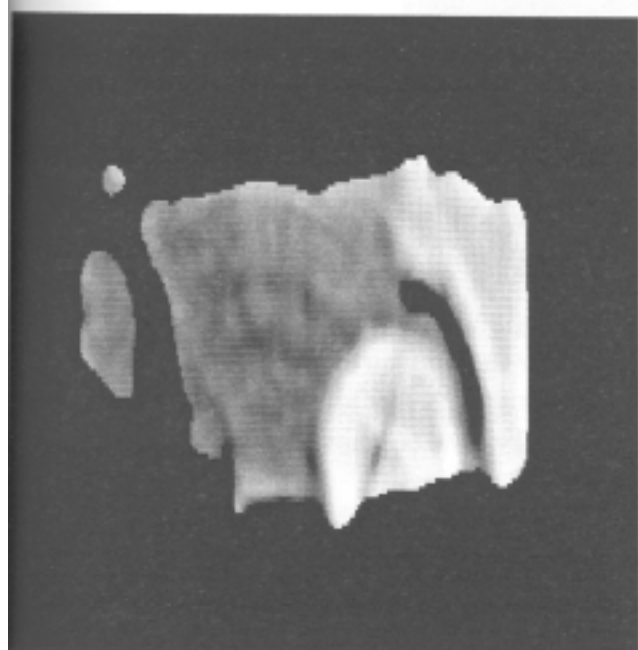
a) Layer 1 image, $c_s = 400$ HU , $w_s = 2500$ HU

b) Layer 2, $c_s = 0$, $w_s = 400$ HU.

c). Z image, $c_s = 9.0$, $w_s = 7.5$.

d) , ρ in g/cm^3, $c_s = 1.2$, $w_s = 0.7$.